

A Certifiable Machine Learning-Based Pipeline to Predict Fatigue Life of Aircraft Structures

Ángel Ladrón^{a,*}, Miguel Sánchez-Domínguez^a, Javier Rozalén^b, Fernando R. Sánchez^b, Javier de Vicente^a, Lucas Lacasa^c, Eusebio Valero^{a,d}, Gonzalo Rubio^{a,d}

^a*ETSIAE-UPM - School of Aeronautics, Universidad Politécnica de Madrid, Plaza Cardenal Cisneros 3, E-28040, Madrid, Spain*

^b*Airbus Defence & Space, Fatigue & Damage Tolerance, Getafe, Spain*

^c*Institute for Cross-Disciplinary Physics and Complex Systems (IFISC), CSIC-UIB, Palma de Mallorca, Spain*

^d*Center for Computational Simulation, Universidad Politécnica de Madrid, Campus de Montegancedo, Boadilla del Monte, 28660, Madrid, Spain*

Abstract

Fatigue life prediction is essential in both the design and operational phases of any aircraft, and in this sense safety in the aerospace industry requires early detection of fatigue cracks to prevent in-flight failures. Robust and precise fatigue life predictors are thus essential to ensure safety. Traditional engineering methods, while reliable, are time consuming and involve complex workflows, including steps such as conducting several Finite Element Method (FEM) simulations, deriving the expected loading spectrum, and applying cycle counting techniques like peak-valley or rainflow counting. These steps often require collaboration between multiple teams and tools, added to the computational time and effort required to achieve fatigue life predictions. Machine learning (ML) offers a promising complement to traditional fatigue life estimation methods, enabling faster iterations and generalization, providing quick estimates that guide decisions alongside conventional simulations. In this paper, we present a ML-based pipeline that aims to estimate the fatigue life of different aircraft wing locations given the flight parameters of the different missions that the aircraft will be operating throughout its operational life. We validate the pipeline in a realistic use case of fatigue life estimation, yielding accurate predictions alongside a thorough statistical validation and uncertainty quantification. Our pipeline constitutes a complement to traditional methodologies by reducing the amount of costly simulations and, thereby, lowering the required computational and human resources.

Keywords: Fatigue Life, Machine Learning, Aerospace Safety, Aerospace Certification, Statistical validation

^{*}Corresponding author.

Email address: `angel.1cordoba@upm.es` (Ángel Ladrón)

List of Acronyms

CFD	Computational Fluid Dynamics
FEM	Finite Element Method
G&M	Gusts and Maneuvers
GAG	Ground Air Ground
MAE	Mean Absolute Error
ML	Machine Learning
MLP	Multilayer Perceptron
MRE	Mean Relative Error
PSE	Principal Structural Element

1. Introduction

Damage estimation caused by fatigue [1] is a critical aspect of aeronautical engineering, as failure to predict it accurately can lead to catastrophic structural breakdowns and compromise both flight safety and operational efficiency. Likewise, fatigue damage assessment is essential for implementing predictive maintenance strategies that extend the life of aircraft and reduce unplanned downtime. Standard fatigue prediction methods rely on a convoluted and resource-intensive process that combines service history of aircraft of similar structural design with aerodynamic and Finite Element Methods simulations and cumulative damage modeling to guide expert-based decision making (CS-25.571 in [2]). The complexity of the whole process makes the development of tailored maintenance routines for new aircraft operators particularly expensive and time-consuming, involving multidisciplinary teams and a range of iterative procedures.

Interestingly, the advent of Machine Learning (ML) techniques and the rapid incorporation of these tools within the aeronautical engineering community (encompassing fields from aerodynamics [3, 4, 5], stress prediction [6] or aeroacoustics [7, 8] to airflow optimization [9] –see [10] for a recent review–) provides a realistic opportunity to streamline and optimize the procedures for fatigue-related damage prediction, as these techniques potentially offer near-instantaneous inference of fatigue life, once properly trained. Specifically in fatigue-related problems, ML has been recently used for load spectrum reconstruction [11, 12], fatigue life prediction [13, 14], and crack growth modeling [15, 16]. However, most approaches treat these steps separately and rely on hybrid frameworks that combine ML with traditional tools, lacking end-to-end ML-enabled fatigue life prediction pipelines.

At the same time, there is an urge of incorporating fully certifiable ML-based procedures within the aeronautical industry. As a matter of fact, a key consideration for ML in safety-critical applications is the ability to certify the predictive model. Aeronautical authorities such as EASA have outlined the main challenges and goals of these industries for trustworthy ML adoption [17, 18], and recent research has started to propose practical methodologies for statistical validation of ML pipelines in industrial settings [6], encompassing data preparation, model training and interpretability, and multiscale uncertainty quantification.

This work proposes a fully integrated and certifiable ML-based pipeline capable of predicting fatigue life at various locations of an aircraft wing, based solely on flight parameters. The pipeline mostly uses a suite of different multilayer perceptrons (MLPs) to approximate different input-output relationships within the fatigue damage assessment. An MLP is an archetypal method in supervised machine learning [19] used to infer (regress or classify) complex input-output representations $x \rightarrow y$, where $x \in \mathbb{R}^m$ and y is usually another vector for regression tasks or an element from a discrete set in classification tasks. Often visualized as an (artificial neural) network, an MLP consists in a (deep) feedforward neural network representing an overparameterized nonlinear function $\mathcal{F}(x; \Omega)$, where $\Omega = \{w_k\}$ –the set of trainable parameters– identify with the weights of the links between neurons (see [19] for details). The precise architecture of the MLP (number of neurons per layer, number of layers) as well as the precise optimization scheme to train the network are defined in a case-by-case basis.

Our approach enables end-to-end learning of the physical process –from stress estimation to load cycle characterization and fatigue damage inference— reducing the need for intermediate, time consuming CFD or FEM simulations. At the same time, the pipeline enforces a statistically solid validation protocol which, overall, aims to pave the way for certifiable ML-driven fatigue assessment. Using real fatigue data from 38 wing locations of a tactical aircraft for different operational profiles, we show that the pipeline provides accurate fatigue life prediction along with a thorough characterization of the model’s uncertainty.

The rest of this paper is structured as follows: in Section 2, we present the full methodology: we define the physical problem under study, the dataset, the set of ML techniques and software tools, and the statistical techniques used for a thorough validation. Then, in Sec. 3 we present the results, which we anticipate yield a successful ML-driven fatigue life prediction tool. Finally, conclusions and future directions are discussed in Sec. 4.

2. Methodology

In this section, we present the methodology adopted in this work. First, in subsection 2.1, we describe the physical problem being modeled using machine learning techniques and explain how it is decomposed into smaller, learnable subproblems. Then, in subsection 2.3, we detail the available dataset and the data-splitting strategy used for training, which plays a crucial role in the performance of the models. Finally, in subsection 2.4, we add a few comments on the ML and statistical software libraries we have used.

2.1. Breaking down the fatigue damage assessment

The goal of this study is to develop a machine learning pipeline to predict fatigue life (expressed as the number of flights to failure) at multiple wing locations –known as principal structural elements (PSEs)–, when flying a specific mission (i.e., a flight characterized by specific flight parameters and operational objectives). In what follows we unfold the process and breakdown the whole supervised learning task in a sequence of interpretable subtasks, see Fig. 1 for an illustration of the different steps.

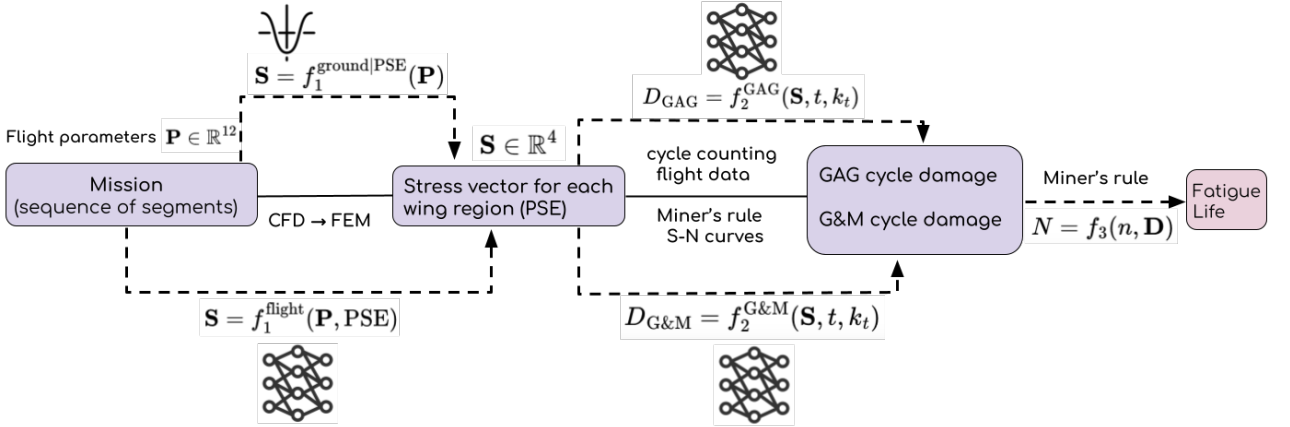


Figure 1: Illustration of the multi-step fatigue-related damage assessment (see the text for details). Our machine learning-based pipeline breaks down the whole process in three phases, where three function families $f_1 = \{f_1^{\text{ground|PSE}}, f_1^{\text{flight}}\}$, $f_2 = \{f_2^{\text{GAG}}, f_2^{\text{G\&M}}\}$, f_3 are approximated with suitable statistical and deep learning models.

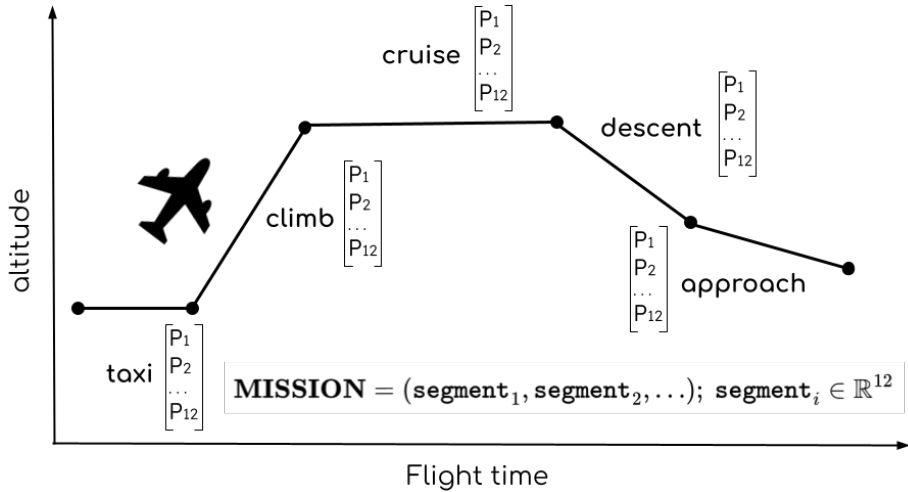


Figure 2: A mission flight plan, partitioned as a sequence of segments. Each segment is parametrized by a 12-dimensional feature vector \mathbf{P} whose elements include variables such as the degree of extension of the flaps in that segment, the true airspeed during the segment, etc (see Table A.10 for details.)

Mission segmentation – The assessment process starts by defining the mission plan (sub-paragraph 6b in CS-25.571, [2]). This process consists in partitioning a mission into a structured sequence of flight segments, see Fig. 2. Each of these segments characterize different specific phases of the flight, so that the categorical variable $\text{SEGMENT} \in \{\text{taxi}, \text{climb}, \text{cruise}, \text{descent}, \text{approach}\}$. It is also useful to classify segments in the **ground**

phase (`taxi`) or in the `flight phase` (every other segment except `taxi`)¹. Accordingly, a mission flight plan is simply represented as a sequence of segments. At the same time, each segment is characterized by a vector of 12 flight parameters $\mathbf{P} \in \mathbb{R}^{12}$, that includes variables such as the degree of extension of the flaps in that segment, the true airspeed during the segment, the altitude at which the segment takes place, and so on (see Table A.10 for details). Accordingly, within each mission, any given flight is described in terms of a sequence of segment feature vectors $\{\mathbf{P}_i\}$ with class metadata (segment class and ground/air typification).

From aerodynamic loads to PSE stresses – Once the mission has been segmented and parameterized, Computational Fluid Dynamics (CFD) simulations are performed in each mission segment to obtain the corresponding aerodynamic loads. These loads are then propagated onto the structural level using Finite Element Method (FEM) simulations, so as to obtain the stresses at the different principal structural elements (PSEs) of interest (appendix 2 in CS-25.571, [2]). The resulting values will be used for the stress spectrum generation. For each PSE, we have a particular four-dimensional stress vector $\mathbf{S} \in \mathbb{R}^4$, whose elements are $\mathbf{S} = (1g, \Delta v_{man}, \Delta v_{gust}, \Delta turn)$, where $1g$ is the mean equilibrium stress at the studied PSE in steady flight (i.e. the structural response under nominal flight conditions), whereas the other three variables are incremental stresses at the studied PSE caused by a standard load factor of $1.5g$ due to vertical maneuvers, vertical gusts and turns. These latter variables capture the effects of atmospheric turbulence and pilot-induced maneuvers (see Table A.11 for details). The incremental stresses values depend on the modeling. To account for gusts, ESDU data or PSD models (CS-25.341 in [2]) can be used and for maneuvers military regulations specify the requirements [20]. This step is computationally intensive and must be repeated for each mission segment individually, making it one of the most resource-consuming parts of the process.

From stresses to GAG and G&M cycles – With the stress data obtained in the previous step and historical flight records from a similar aircraft, two types of load cycles are derived for each mission: the so-called Ground-Air-Ground (GAG) cycle and the cycles induced by gusts and maneuvers. The GAG cycle represents the dominant stress fluctuation experienced as the aircraft transitions from ground to flight segments. This cycle typically involves the largest stress amplitude of the flight (minimum to maximum stress) and occurs once per flight. In contrast, gusts and maneuvers generate multiple smaller cycles within each flight segment. These are constructed using statistical load distributions and serve as an approximation of the fatigue loads that the aircraft will encounter across all the mission flights. Each resulting cycle is represented as a triplet: the maximum stress, the minimum stress, and the number of times that specific cycle occurs. Together, the cycles induced by gusts and maneuvers, along with the GAG cycle (derived from them) constitute the two main

¹While in rigor there exist ground segments other than `taxi` (e.g. `take-off`, `braking`, `rotation`, etc), these are not explicitly taken into account in the models as the wing PSEs don't show any significant damage induced by these type of segments.

sources of fatigue damage—typically with the GAG cycle being the dominant contributor.

Final assessment of fatigue life – Once the load cycles have been defined, the fatigue damage and corresponding life of the structural component can be estimated using material properties and local stress information. A key input in this step is the so-called S–N curve, which describes the relationship between the stress (typically the stress amplitude) and the number of cycles to failure for a given material and stress concentration factor, k_t . The factor k_t quantifies how much the local stress is amplified due to defects or geometric features such as holes, fillets, or notches. Based on these parameters, along with the load history, the mission definition and the principal structural element (PSE), the fatigue life, quantified as number-of-flights-to-failure N , can be formally expressed as:

$$N = \mathcal{F}(\text{material}, k_t, \text{historical data}, \text{PSE}, \text{mission data}, \text{stress data}). \quad (1)$$

A linear damage accumulation model (Miner’s rule [21]) is finally adopted to estimate fatigue damage. The core idea is that the damage caused by each stress cycle is independent and additive, and thus the total damage is simply the sum of these contributions. Under this model, the damage \mathcal{D} accumulated after n flights per mission is simply given by:

$$\mathcal{D} = \frac{n}{N}, \quad (2)$$

such that by definition, failure occurs when the number of flights reaches the critical value $n^* = N$, i.e. at $\mathcal{D} = 1$. Although this model simplifies the effects of plasticity and the interactions between loads, it remains widely used in aerospace applications and serves as the reference for ground truth values in this study.

2.2. Fatigue life prediction using Machine Learning

As previously outlined, fatigue life estimation relies on a sequential process that demands substantial computational and human resources. It typically requires a combination of high-fidelity CFD and FEM simulations, followed by load cycle reconstruction and counting techniques. This workflow is not only time-consuming but also difficult to scale. In contrast, machine learning offers the potential for near-instantaneous inference and significant reductions in both computational cost and operational complexity, hence the opportunity. The rationale starts from assuming that $\mathcal{F}()$ in Eq. 1 is a deterministic function, and aim to approximate it using a suite of ML models. Now, after preliminary inspection it was clear that modeling \mathcal{F} with a single neural network led to stagnant loss curves and suboptimal learning. This, together with the fact that including every step of the process into a single neural network hinders interpretability, led us to reformulate the solution as a sequential pipeline composed of three supervised learning (regression) tasks, such that the global task (approximate \mathcal{F} in Eq. 1) can be seen as a function composition, i.e. conceptually we have $\mathcal{F} = f_3 \circ f_2 \circ f_1$, where f_1 , f_2 and f_3 are nonlinear functions mapping different stages of the fatigue damage assessment pipeline described in Fig. 1. As we shall see, each of these functions are approximated by different ML and statistical models.

As in the traditional approach, the ML pipeline begins by translating the mission into a

structured sequence of flight segments, each described by 12 constant flight parameters. These parameters capture the operational characteristics of the aircraft during each segment (e.g., taxi, climb, cruise) and serve as input features for the first stage of the pipeline. For each {mission, PSE} pair, the pipeline proceeds in three phases:

- **Phase I – Stress prediction:** The objective of this phase is to predict the stress vector $\mathbf{S} \in \mathbb{R}^4$ at each principal structural element (PSE) and for every mission segment, using the corresponding flight parameters $\mathbf{P} \in \mathbb{R}^{12}$ as input. Details on the components of \mathbf{P} and \mathbf{S} are provided in Appendix A.1.

Formally, this task involves learning a function f_1 such that

$$f_1 : \mathbb{R}^{12} \rightarrow \mathbb{R}^4, \quad \mathbf{S} = f_1(\mathbf{P}, \text{PSE})$$

where the mapping is conditioned on the PSE under study. To account for the distinct physical regimes involved, we unfold f_1 into two separate models $f_1^{\text{ground|PSE}}$ and f_1^{flight} that model f_1 for ground and flight segments, respectively. Ground segments, dominated by static loads (e.g., fuel weight), exhibit relatively simple stress responses and therefore we chose $f_1^{\text{ground|PSE}}$ to be a different second-order polynomial model for each PSE, with only one input variable (fuel weight) and a single output variable (1g). In contrast, flight segments involve dynamic aerodynamic loading, requiring more flexible functional shapes. Accordingly, f_1^{flight} is approximated by a multilayer perceptron (MLP). After feature selection, we keep six out of the 12 features in \mathbf{P} as input variables, and we add an encoding of the PSE as an additional independent variable, i.e. a single MLP was trained to generalize across all flight segments and wing locations. The output of this MLP is the full, four dimensional stress vector \mathbf{S} (additional details on model architecture, input selection, and preprocessing for f_1^{flight} are provided in Appendix A).

- **Phase II – Damage prediction:** The second phase of the pipeline estimates, from the stress data, the fatigue damage accumulated at each PSE over n flights of a given mission. Since the particularities of each PSE are already encoded in the different stresses, PSE is not anymore an input variable at the stage. Now, there are two distinct damage components: \mathcal{D}_{GAG} , the damage caused by the Ground–Air–Ground (GAG) cycle after n flights, and $\mathcal{D}_{\text{G\&M}}$, the damage induced by gusts and maneuver loads during flight segments after n flights. These are the two primary contributors to fatigue degradation in metallic aircraft structures. Since they are distinct, we separate the analysis and consider two separate tasks:

(i) The first task is that of predicting the per-flight damage caused by the Ground–Air–Ground (GAG) cycle \mathcal{D}_{GAG} . This prediction uses as input variables the average stress values during ground and flight segments $\bar{\mathbf{S}}_{\text{ground}} \in \mathbb{R}$ and $\bar{\mathbf{S}}_{\text{flight}} \in \mathbb{R}^4$ (computed from the Phase I stress predictions), along the time the aircraft spends in flight and on the ground during a single flight, $t_{\text{ground}}, t_{\text{flight}} \in \mathbb{R}$ and the stress concentration factor, $k_t \in \mathbb{R}$ (see Appendix B for details). In principle this is a per-flight quantity and

thus independent of n . However, although n is large ($n \in [800, 13,000]$) and the average damage is expected to asymptotically converge to the true per-flight value-as per the law of large numbers-we also add n as an input variable, to account to possible deviations from the true mean due to finite samples effects. Mathematically

$$f_2^{\text{GAG}} : \mathbb{R}^9 \rightarrow \mathbb{R}, \quad \overline{\mathcal{D}_{\text{GAG}}} = f_2^{\text{GAG}}(\bar{\mathbf{S}}_{\text{ground}}, \bar{\mathbf{S}}_{\text{flight}}, t_{\text{flight}}, t_{\text{ground}}, k_t, n).$$

The total GAG-related damage after n flights $\mathcal{D}_{\text{GAG}} = \overline{\mathcal{D}_{\text{GAG}}} \cdot n$.

(ii) Likewise, the second task is that of predicting the the per-flight damage caused by the Gusts and Maneuvers (G&M) cycles $\overline{\mathcal{D}_{\text{G\&M}}}$. This prediction uses the same inputs as before, except for the ground-related variables. Mathematically, we have

$$f_2^{\text{G\&M}} : \mathbb{R}^7 \rightarrow \mathbb{R}, \quad \overline{\mathcal{D}_{\text{G\&M}}} = f_2^{\text{G\&M}}(\bar{\mathbf{S}}_{\text{flight}}, t_{\text{flight}}, k_t, n).$$

The total G&M-related damage after n flights $\mathcal{D}_{\text{G\&M}} = \overline{\mathcal{D}_{\text{G\&M}}} \cdot n$

We train two different MLPs to approximate f_2^{GAG} and $f_2^{\text{G\&M}}$. Note that the use of averaged stress values instead of segment-wise cycle estimation is motivated by the high variability of load spectra across flights and the lack of deterministic predictability of individual stress cycles. Since missions typically involve a large number of flights ($n \in [800, 13,000]$), this formulation is justified by the Central Limit Theorem and the assumption of independent (Miner's rule), identically distributed flights. Both models were trained using log-transformed damage values to address the wide dynamic range in the output space, and we use a Mean Absolute Error (MAE) loss function to penalize poor performance on high-damage cases, which are the most critical in fatigue life estimation. Full details on the data preparation, feature engineering, model architecture and split strategy are provided in Appendix B.

- **Phase III - Life prediction:** The final phase computes the fatigue life N defined as the number-of-flights-to-failure for a given mission and PSE. The model takes as inputs the number of flights, n , and the two sources of accumulated fatigue damage $\mathcal{D}_{\text{GAG}}, \mathcal{D}_{\text{G\&M}}$ predicted in Phase II, such that $N = f_3(\mathcal{D}_{\text{GAG}}, \mathcal{D}_{\text{G\&M}})$. Rather than approximating f_3 via an additional ML model, we instead apply the simpler Miner's rule directly, as described in subsection 2.1. This linear damage accumulation model assumes failure occurs when total damage reaches unity. Accordingly, fatigue life is computed as:

$$N = f_3(n, \mathcal{D}_{\text{GAG}}, \mathcal{D}_{\text{G\&M}}) = \frac{n}{\mathcal{D}_{\text{GAG}} + \mathcal{D}_{\text{G\&M}}}. \quad (3)$$

2.3. Dataset and split description

Our dataset contains information regarding 38 wing PSEs, labeled 1, 2, … to 38, four different k_t values, and seven different missions operated by a specific certification of the studied tactical aircraft, labeled A, B, … to G. Each mission represents accumulated data over a large number of flights, typically ranging between $n \in [800, 13000]$.

As stated in subsection 2.1, fatigue damage assessment requires conducting different steps (Figure 1), such as running FEM simulations, load cycles construction and finally, computing damage (and life) with the S-N curves. Our database, contains the output of each one of these steps, which will serve as the ground truth values for our ML approach.

As previously discussed, missions are divided into operational segments such as `taxi`, `climb`, `cruise`, `descent`, and `approach`, being each mission segment described in the dataset by 12 scalar flight parameters collected into a vector $\mathbf{P} \in \mathbb{R}^{12}$. These flight parameters induce certain stresses at each PSE (FEM output), represented by 4-dimensional stress vectors $\mathbf{S} \in \mathbb{R}^4$, which represent the local stress at the component for different loading conditions. Details about \mathbf{P} and \mathbf{S} provided in subsection Appendix A.1. We leverage this data to address phase I from subsection 2.1.

In addition, for all the missions, the load cycles induced by gusts and maneuvers during every segment, derived from statistical load distributions (subsection 2.1), are available at each PSE, along with the GAG cycles and the respective fatigue damages (for the four k_t values) accumulated over n flights of the respective mission. The ground truth of fatigue life is easily computed with these damages.

Data split – Instead of performing a random split on all the $38 \times 7 \times 4 = 1064$ {PSE, Mission, k_t } combinations- which could result in data leakage and in some PSEs being absent from the test set -the following split was performed. For each PSE, a set of five out of the seven missions have been randomly selected for the training set (for the four k_t values, treated as numerical variables), one mission for the validation set and another mission for the test set. The validation set is used for hyperparameter tuning while the test set is used to assess the overall performance of the pipeline. Details on how this split is applied in each phase are provided in subsection Appendix A.2 and subsection Appendix B.3.

2.4. Note on software

ML models were developed using `pyLOM` [22], a high-performance computing-enabled framework for parallel reduced-order modeling implemented in PyTorch [23]. In addition, we also used standard Python libraries, such as `scikit-learn` [24] for polynomial regression and data preprocessing, `pandas` [25] and `NumPy` [26] for dataset manipulation, and `matplotlib` [27] for visualization.

3. Results

In this section, we start by presenting the results of every step of the pipeline f_1, f_2, f_3 , along with a thorough error quantification of each of the predictions. The relative error used throughout this section is the absolute percentage error:

$$\text{Relative Error (\%)} = \left| \frac{\hat{y} - y}{y} \right| \times 100, \quad (4)$$

where \hat{y} and y are the predicted and true values respectively.

3.1. Phase I: Stress predictions

First, we will study the results of the stress vector \mathbf{S} predictions of every mission segment and for every PSE \in Test set. This phase approximates f_1 in Fig. 1.

	Mean Relative Error (%)	Std	Q1	Q2	Q3
1g	0.04	0.03	0.019	0.03	0.06

Table 1: Relative Error statistics for \mathbf{S} predictions for ground segments, displaying the mean relative error (relative error averaged over all PSEs and ground segments), the standard deviation, and the first three quartiles.

Ground segments: $f_1^{\text{ground|PSE}}$ – As stated in subsection 2.1, the predictions of the stress vector for ground segments (taxi) were addressed with second order polynomial regression models $f_1^{\text{ground|PSE}}$. As detailed in Appendix A, after an initial feature selection we decide to use just one of the 12 flight parameters –namely, fuel weight $FW \in \mathbb{R}_+$. Likewise, for ground segments the only output variable is the equilibrium stress $1g \in \mathbb{R}$. Accordingly, for each PSE, $1g = f_1^{\text{ground|PSE}}(FW)$, where $f_1^{\text{ground|PSE}}$ is a simple quadratic polynomial such as:

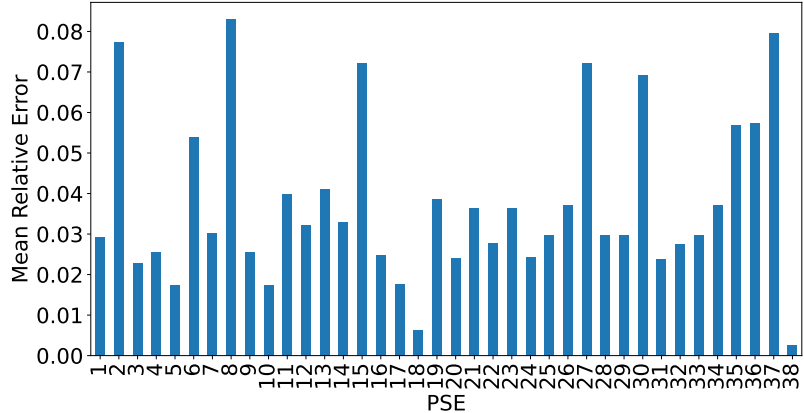
$$f_1^{\text{ground|PSE}}(FW) = \beta_0 + \beta_1 FW + \beta_2 FW^2,$$

where β_0 , β_1 and β_2 are the polynomial coefficients, obtained by minimizing the residual sum of squares between predictions and ground truth values (ordinary least squares) [24].

First, in Table 1 we display the statistics of the relative error for the $1g$ stress prediction in the test set. The mean relative error (MRE) –i.e. the relative error averaged over all ground segments and PSEs– is substantially below 1%, indicating a very good performance. To gain insight on the dependency of the prediction error on the PSEs and missions, we depart from pointwise statistics and in Fig. 3 we plot the Mean Relative Error (MRE) of the $1g$ stress predictions conditioned on (i.e. grouped by) PSEs. As observed, although there is a slight variability in performance between PSEs, for all PSEs the MRE systematically remains below 0.1%. Similarly, Table 2 shows the performance (again in terms of MRE) but now grouped by missions instead of PSEs. As observed, all the missions exhibit excellent performance and again, MRE systematically remains below 0.1%. Overall, these results indicate that the dependence of the $1g$ stresses on flight parameters for ground segments is very simple and is well captured by a second order polynomial.

	A	B	C	D	E	F	G
1g	0.05	0.05	0.03	0.02	0.04	0.04	0.05

Table 2: MRE for the predictions of each element of the stress vector \mathbf{S} over ground segments, grouped per mission class.



visualizing some of the flight parameter histograms for mission A, as compared to the rest of missions. This data is depicted in Fig. 6, where we observe that for some of the flight parameters (altitude and some mass-related parameters), mission A’s distributions deviate from the bulk for some segments, i.e. they are located in a poorly sampled region of the input space, a well-known reason for poorer generalization [6].

	MRE (%)	Std	Q1	Q2	Q3
$1g$	0.86	0.89	0.29	0.63	1.06
Δv_{man}	0.48	0.50	0.14	0.33	0.68
Δv_{gust}	0.73	0.66	0.25	0.56	1.03
$\Delta turn$	1.17	1.05	0.40	0.87	1.60

Table 3: Relative error statistics for the predictions of all four elements of the stress vector \mathbf{S} over flight segments: mean relative error (MRE, %, averaging over all PSEs and flights segments), standard deviation, and the first three quartiles Q1 (percentile 25), Q2 (median) and Q3 (percentile 75).

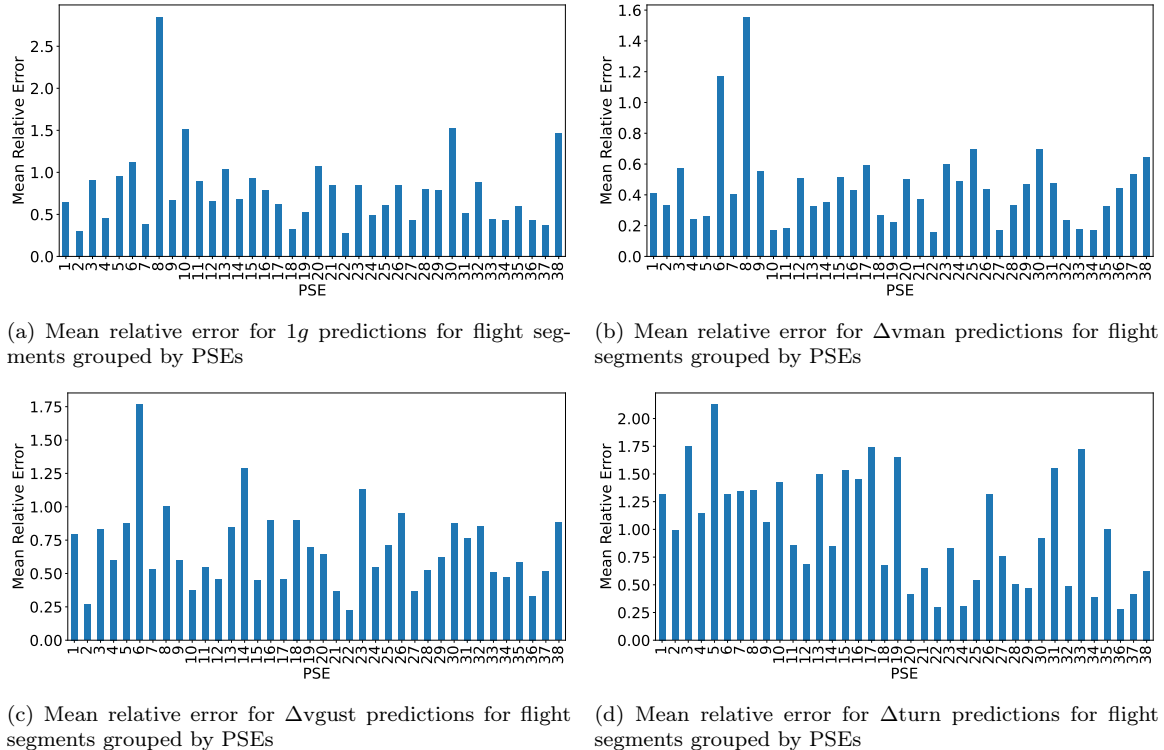


Figure 5: Mean relative error grouped by PSEs for the all the predicted stresses

Modeling this first phase of the pipeline with $\{f_1^{\text{ground|PSE}}, f_1^{\text{flight}}\}$ has demonstrated good accuracy. The output of these models will serve to build the input for the following steps of

Mission	A	B	C	D	E	F	G
$1g$	1.12	0.60	0.79	0.66	0.65	0.65	0.66
Δv_{man}	0.68	0.37	0.36	0.42	0.41	0.42	0.30
Δv_{gust}	0.90	0.52	0.68	0.70	0.53	0.69	0.57
Δt_{turn}	1.29	0.56	1.66	0.97	0.48	0.64	0.75

Table 4: MRE per mission for \mathbf{S} predictions over flight segments

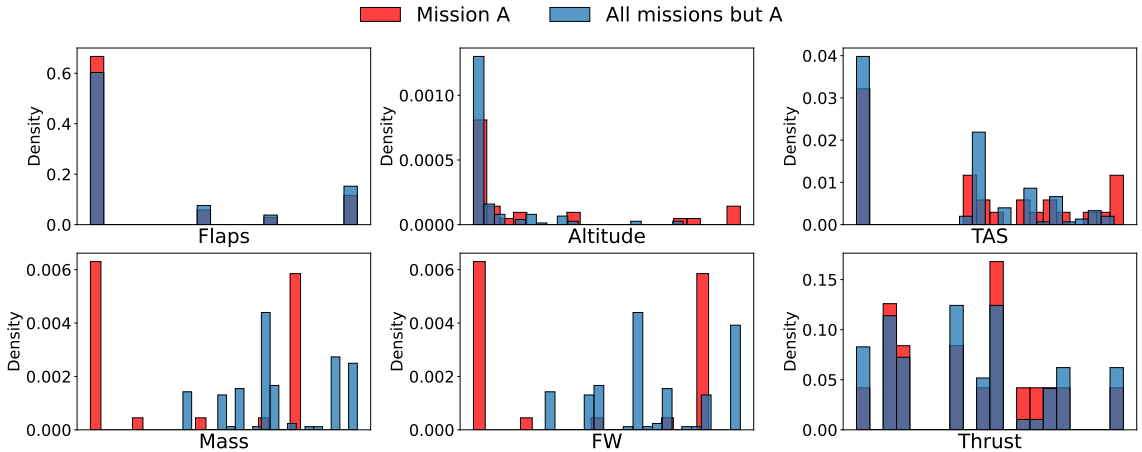


Figure 6: Histograms of input variables for mission A vs all the other missions. Specific support ranges have been hidden for confidentiality reasons.

the pipeline. Observe that the small errors in the prediction of stress vectors will propagate into phase II prediction.

3.2. Phase II: GAG and G&M Damage prediction

In this phase, both sources of fatigue damage are predicted separately with two different MLP models, that approximate f_2^{GAG} and $f_2^{\text{G\&M}}$ respectively. In Fig. 7 the learning curves of the models are depicted. They were trained for 5000 epochs (note that working with mini-batches results in many iterations per epoch). As observed, during the training process, the validation loss remains close to the training loss (MAE) for both models. The gusts and maneuvers damage model shows a more noisy learning process than the GAG damage model, but still manages to learn. Finally, the validation sets remain flat, so extending the training for more epochs might lead to a high-variance scenario, where the model would learn spurious noise.

In Table 5 and Table 6 we show a summary of the relative error (%) statistics of the damage predictions \mathcal{D}_{GAG} and $\mathcal{D}_{\text{G\&M}}$, for all the points in the test set. As we can see, the mean relative error is moderately large and substantially larger than the median, what suggests a skewed, fat-tailed error distribution. Notice, indeed, that the third quartile is not symmetric

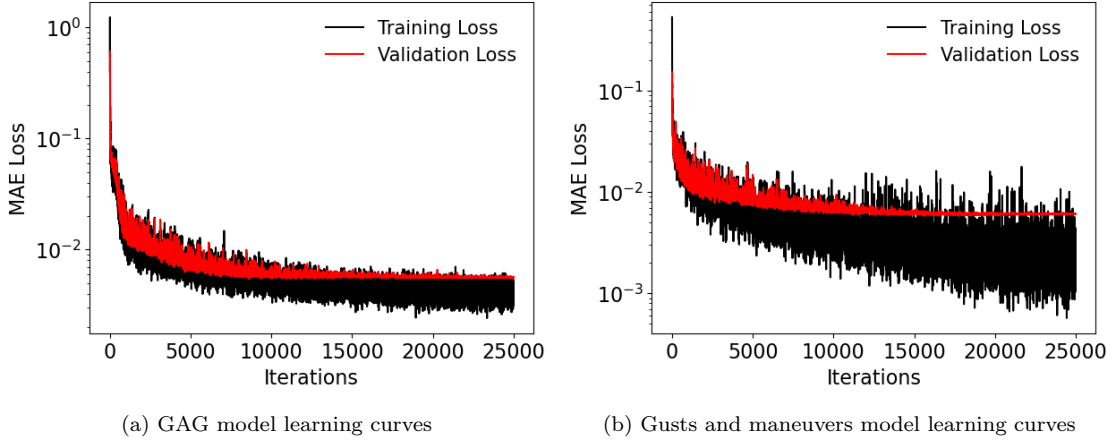


Figure 7: Learning curves for both damage models approximating (a) f_2^{GAG} and (b) $f_2^{\text{G\&M}}$.

with respect to the first quartile, and that the max error is disproportionately large. This suggests that pointwise error statistics are being deformed –and the average performance apparently decreased– due to the presence of outliers. So it is important to ascertain where these outliers are located. Since the models predict fatigue damage –which can lead to instantaneous breakage–, greater damages represent more critical situations in both cases, as fatigue failure will be achieved earlier, resulting in shorter fatigue lives. Therefore, it is in the high-damage region that the MLP models must be more accurate, and therefore we need to certify that outliers are never present in this region.

Relative error stats	Values
Mean	8.12
Standard deviation	12.10
First quartile (25%)	1.21
Median (50%)	3.67
Third quartile (75%)	9.40
Min error	0.08
Max error	80.95

Table 5: Relative error statistics for the prediction of \mathcal{D}_{GAG} .

Relative error stats	Values
Mean	9.49
Standard deviation	21.80
First quartile (25%)	2.47
Median (50%)	4.94
Third quartile (75%)	8.40
Min error	0.03
Max error	202.29

Table 6: Relative error statistics for the prediction of $\mathcal{D}_{\text{G\&M}}$.

Now, recall that we are using the mean absolute error (MAE) as the loss function in both cases

$$\mathcal{L}_{\text{MAE}} = \frac{1}{m} \sum_{i=1}^m |y_i - \hat{y}_i|, \quad (5)$$

where m are the number of samples on the mini batch and y_i , \hat{y}_i are the generic true and predicted damages, respectively. By construction, this loss function already penalizes error

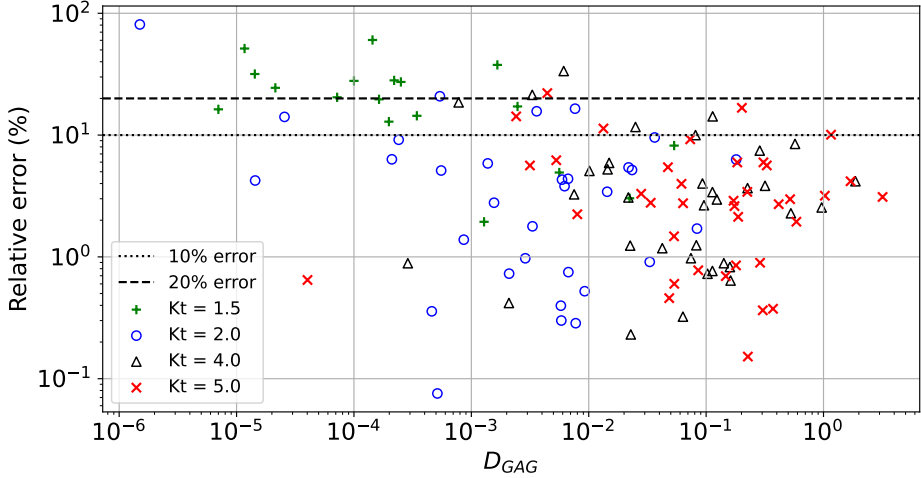


Figure 8: Scatter plot of the relative error of \mathcal{D}_{GAG} as a function of its ground truth value, for every point in the test set.

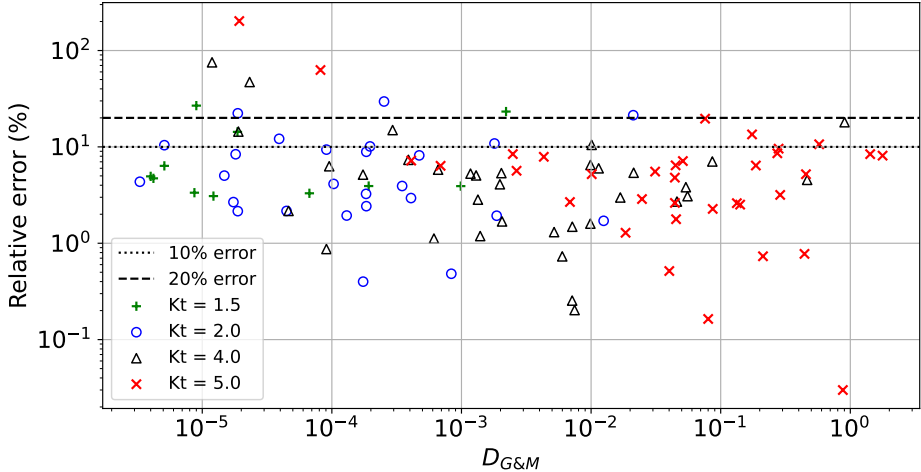


Figure 9: Scatter plot of the relative error of $\mathcal{D}_{G\&M}$ as a function of its ground truth value, for every point in the test set.

for higher damages than for lower damages. To confirm this dependence of the prediction's error on the actual damage, in Figure 8 and Figure 9 we plot, in log-log scales, the relative error for the prediction of accumulated damages \mathcal{D}_{GAG} and $\mathcal{D}_{G\&M}$ as a function of their ground truth values. Each point in these two scatter plots represents a $\{\text{Mission}, \text{PSE}, k_t\} \in \text{Test set}$. Clearly, model's performance is better in the region of high damages (region of interest), and it is in the region of low damages that the error outliers tend to concentrate (observe that the plots are logarithmic). This bias is even stronger for the GAG damage predictions –which is actually the main source of fatigue damage of the studied aircraft–, showing a statistically significant weak inverse correlation between the accumulated damage

and the relative error of the prediction (Spearman’s $\rho = -0.353$ with $p\text{-value} = 6.7 \times 10^{-5}$). In contrast, for the accumulated damage caused by gusts and maneuvers, the correlation is very weak and not statistically significant (Spearman’s $\rho = -0.17$ with $p\text{-value} = 0.085$). However, the distribution outliers (e.g., following Tukey fences, those points with relative error larger than $Q3 + 1.5IQR = 17.3\%$) are mainly located in the low-damage range.

3.3. Phase III: Fatigue life results

Miner’s Rule is finally applied to obtain total fatigue damage after the n flights, and with Equation 3 fatigue life N can easily be calculated. Since the MLP models for f_2^{GAG} and $f_2^{\text{G\&M}}$ showed better performance for higher fatigue-related damages, errors propagate and thus we expect to get more accurate predictions of fatigue life for shorter to medium fatigue lives, $N \in (10^3 - 10^6)$ - which are the most critical situations- since $N \propto \mathcal{D}^{-1}$.

In Figure 10 we scatter plot the the relative error of each fatigue life prediction N as a function of its ground truth values. It is clear that the model shows a good performance in the region of interest (short to medium fatigue lives). Note that the behavior is similar to that of the inverse of Figure 8. This is expected as the main source of damage for the studied aircraft lies in the GAG cycle.

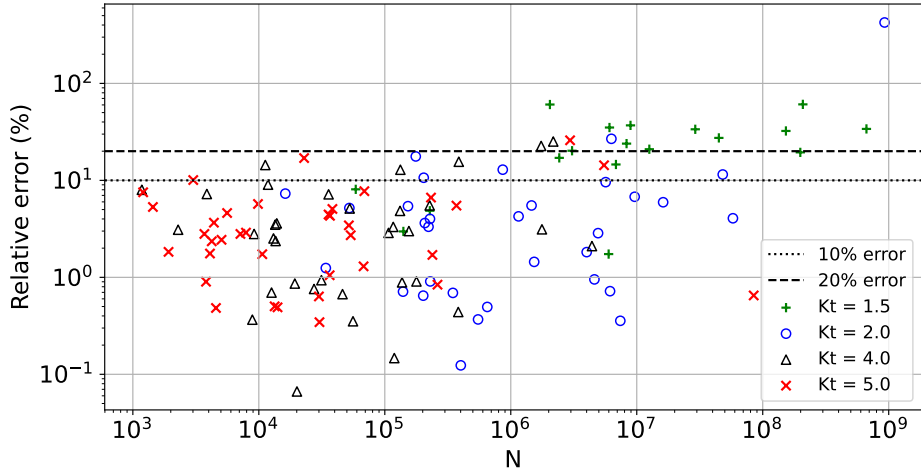
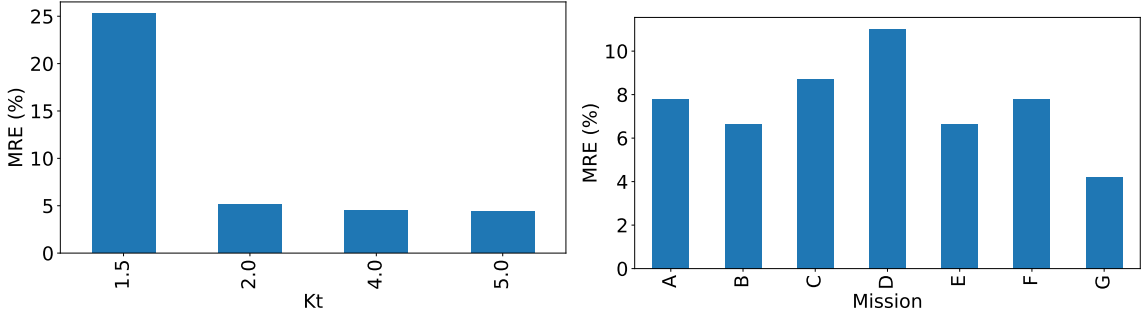


Figure 10: Scatter plot of the relative error of fatigue life prediction as a function of its ground truth value, for every point in the test set.

For completeness, in Figure 11 we also show the mean relative error of fatigue life prediction conditioned on k_t , mission and PSE, respectively. As observed in Figure 11a, cases with smaller k_t concentrate larger relative error. This is a sensible result: small k_t values in general tend to have longer fatigue lives (i.e. the region where the ML model performs worse) because in these cases the local maximum stress is barely amplified by defects or geometry characteristics. Likewise, in Figure 11c we observe that some PSEs show poorer fatigue life prediction, but this is simply because these are subjected to lower stresses, leading to higher fatigue lives and thus poorer model’s performance. Incidentally, note that PSE 15

was not included in the plot as its high error was off-scale. Finally, Figure 11b shows only slight variability in performance across missions.



(a) MRE of fatigue life prediction N , for all test set data grouped by their k_t values. (b) MRE of fatigue life prediction N , for all test set data grouped by their mission class.

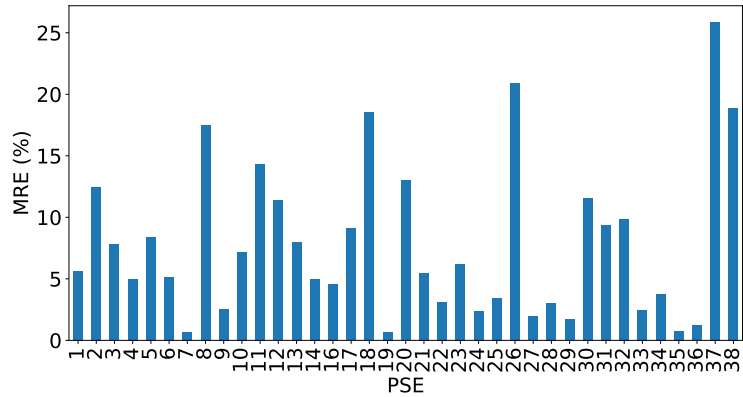


Table 7: Full domain

Relative error stats	Values
Mean	11.37
Standard deviation	39.48
First quartile (25%)	1.05
Median (50%)	3.60
Third quartile (75%)	9.02
Min error	0.07
Max error	424.89

Table 8: Region of usage: $N \in (10^3, 10^6)$

Relative error stats	Values
Mean	3.99
Standard deviation	4.03
First quartile (25%)	0.88
Median (50%)	2.88
Third quartile (75%)	5.34
Min error	0.067
Max error	17.65

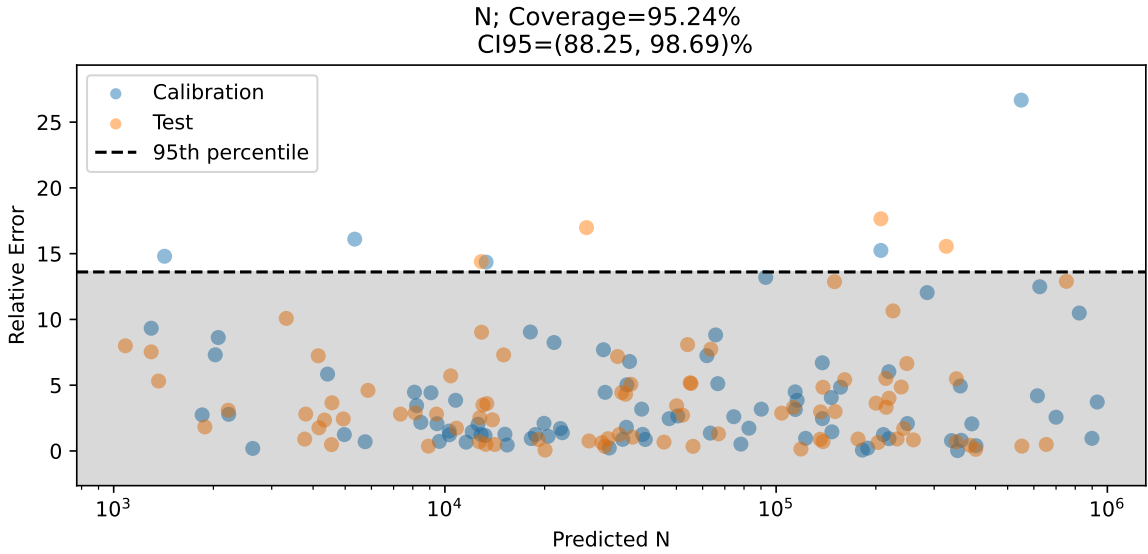


Figure 12: Prediction interval for the relative error

construct bootstrapped CI95 confidence interval of 95th percentile of this metric [6]. In Figure 12 we plot the bootstrap average of this percentile, such that the range $[0, \bar{P}95]$ in principle covers roughly the relative error of about 95% of the points in the calibration and test set. The analysis showed that, using the validation set described in subsection 2.3 as the calibration set to build a prediction interval for the 95% coverage, we achieve a coverage in the test set of 95.24%, CI95 [88.25, 98.69]. This corresponds to an upper bound of the relative error of 13.50%.

Consequently, when predicting the life of a new, previously unseen sample, the true fatigue life can be assured to be $N \in [\hat{N}(1-\varepsilon), \hat{N}(1+\varepsilon)]$ — where $\varepsilon = 0.135$, and \hat{N} is the predicted fatigue life — with approximately 95% confidence.

3.5. A posteriori training/test split analysis

Before assessing the performance of the different ML models, it is a good practice to check whether the training/test data split is adequate, as incorrect splits can be a source of p-hacking—which misleadingly amplifies the performance on the test set—or poor generalization [6]. Now, since in this work the output data of model f_1 is the input data of model f_2 , we now perform such data split analysis a posteriori, and focus in the input data of MLP models f_2 and f_3 , as the configuration space is smaller than the one for f_1 (note that this analysis was performed for all steps):

$$N = f_3(n, \overline{\mathcal{D}_{\text{GAG}}}, \overline{\mathcal{D}_{\text{G\&M}}}) = f_3(n, f_2(\bar{\mathbf{S}}_{\text{flight}}, \bar{\mathbf{S}}_{\text{ground}}, t_{\text{flight}}, t_{\text{ground}}, k_t, n)),$$

where $f_2 = \{f_2^{\text{GAG}}, f_2^{\text{G\&M}}\}$. Following [6], we consider a split to be adequate if (i) finding the same data samples appearing in both the train and test sets has vanishingly small probability, (ii) the feature vector distributions of both sets are similar, and (iii) the test set data is adequately close from the training set.

Criterion (ii) is checked by performing 2-sample hypothesis tests (2-sample Kolmogorov-Smirnov [28], 2-sample Anderson-Darling [29] and 2-sample chi-2 tests) on marginal training and test distributions for each input variable. Criterion (iii) is implemented in the so-called tesselation and proximity method [6], by detecting test set points that are either excessively close (statistically speaking) to the training set (source of p-hacking), or statistically too far (isolated points with poor generalization).

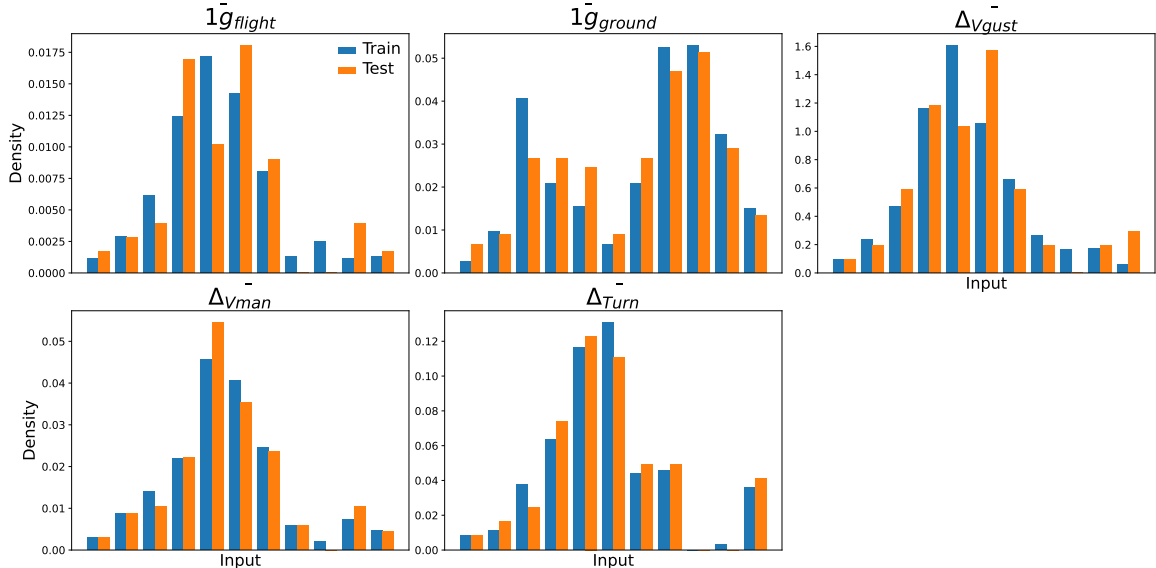


Figure 13: Training vs test marginal distributions for each numerical input variable.

In Figure 13 we plot the marginal training and test set distributions for each numerical input variable, whereas in Figure 14 we plot the ones for the categorical variables. Although

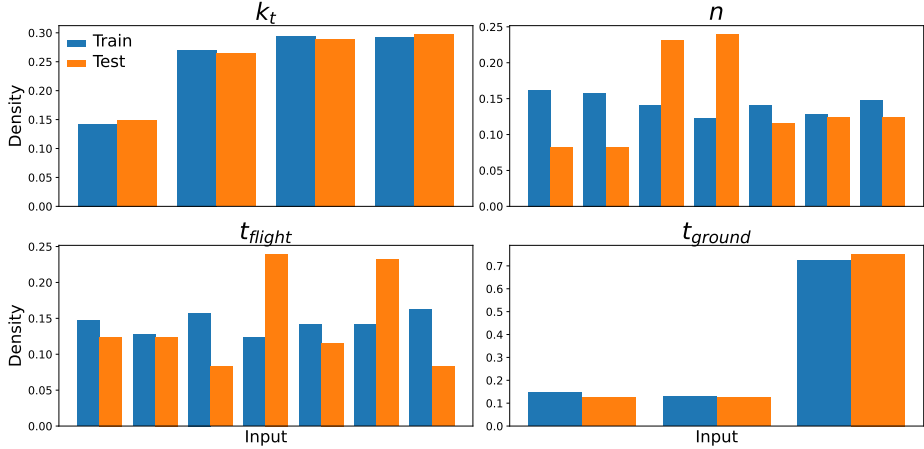


Figure 14: Training vs test marginal distributions for each categorical input variable.

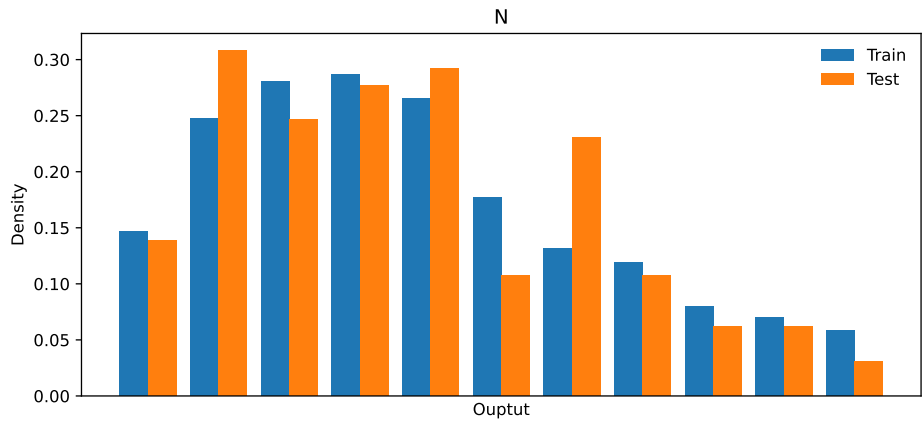


Figure 15: Training vs test marginal distributions for the output variable N .

variables in Figure 14 are actually numerical, for the sake of this analysis they are treated as categorical as they only take a small set of possible values. Therefore, they cannot be considered continuous and a different test is applied (χ^2). Likewise, Figure 15 presents the marginal training and test distributions for the output variable N . Visually, the training and test distributions are similar, although small differences exist. To quantify the significance of these, we have run several hypothesis tests, where the null hypothesis H_0 is that, for each variable, each pair of populations are drawn from the same distribution. Since each hypothesis test has its own null hypothesis, no correction for multiple testing is required, and we adopt the standard choice for rejecting the null. In Table 9 we present the p-values of these tests, where the null hypothesis cannot be rejected for any variable except for n and t_{flight} . Note nonetheless that, as observed in Figure 14, the range values for these two variables is similar in both sets, indicating that at least there are no isolated values in n or t_{flight} in the test set.

Besides, from the 121 samples in the test set, the proximity method flagged three points (2.48% of the test set) as p-hacking and eight as isolated samples (6.6% of the test set). As expected, the p-hacking points showed overly optimistic predictions, with a mean relative error of 0.76%, whereas this value for the isolated points is 10.21%.

Finally, we can conclude that the test set is a good representation of the training set in both the input and output spaces and that the split is adequate, hence providing further assurance that the error and uncertainty quantification developed in previous sections represents well the performance of the model.

Test	k_t	$\bar{1}g_{flight}$	$\bar{1}g_{ground}$	$\bar{\Delta V_{gust}}$	$\bar{\Delta V_{man}}$	$\bar{\Delta T_{turn}}$	n	t_{flight}	t_{ground}	N
KS	-	0.49	0.25	0.08	0.89	0.38	-	-	-	0.95
AD	-	0.25	0.25	0.25	0.25	0.25	-	-	-	0.25
χ^2	1.00	-	-	-	-	-	0.001	0.001	0.92	-

Table 9: p-values for the two-sample Kolmogorov-Smirnov, Anderson-Darling and χ^2 tests, comparing the empirical distribution of each input and output variables in the training vs test sets. Results indicate that, except for n and t_{flight} , for the rest of input variables the null hypothesis of equal distribution cannot be rejected.

4. Conclusions

This study presents a modular machine learning-based pipeline for fatigue life prediction at different wing locations, across multiple stress concentration factors (k_t), using mission-level flight parameters as input. The framework offers a fast, scalable, and accurate complement to traditional simulation-based approaches, with direct applications in early-stage aircraft design, mission planning, and maintenance strategies. The pipeline combines expert-domain feature engineering with deep learning models tailored to flight and ground segments. Once trained, it enables instant fatigue life and damage predictions which turn to be particularly accurate in the medium-to-low fatigue life regime, which is the critical regime for design decisions. The use of predicted stress components as intermediate variables supports both accuracy and physical interpretability. The pipeline has been statistically validated, making it consistent with ongoing initiatives to create certifiable ML tools in safety-critical aerospace systems.

Looking ahead, while the current study is limited to wing components due to data availability, the methodology is extensible to other materials and aircraft structures, such as the fuselage and stabilizers. Future work should also focus on broader structural coverage, improved stress modeling, and further integration of uncertainty quantification conditioned on input space [6].

In summary, the proposed approach represents a novel and effective contribution to fatigue life modeling, demonstrating the feasibility of using machine learning to complement and accelerate conventional analysis pipelines in aerospace structural integrity.

Acknowledgments – The authors acknowledge funding from project TIFON (PLEC2023-010251) funded by MCIN/AEI/10.13039/501100011033, Spain. LL acknowledges partial support from projects MISLAND (PID2020-114324GB-C22), CSxAI (PID2024-157526NB-I00) and MdM Seal of Excellence (CEX2021-001164-M) funded by MICIU/AEI/10.13039/501100011033 and from the European Commission Chips Joint Undertaking project No. 101194363 (NE-HIL). Finally, all authors gratefully acknowledge the Universidad Politécnica de Madrid (www.upm.es) for providing computing resources on Magerit Supercomputer.

Appendix A. Additional details for Phase I

Appendix A.1. Flight parameters and stress vectors

Each segment is parametrized by 12 scalar flight parameters, collected in a vector $\mathbf{P} \in \mathbb{R}^{12}$ whose element description is detailed in Table A.10. We will use these parameters to raise the input of this phase. On the other hand, for each of the 38 wing locations (PSEs), stress variables are collected in a four-dimensional stress vector $\mathbf{S} = (1g, \Delta v_{man}, \Delta v_{gust}, \Delta \text{turn})$, which represents the local stress at the component for different loading conditions. The physical meaning of each variable in \mathbf{S} is detailed in Table A.11. Note that for ground segments $\Delta v_{man} = \Delta v_{gust} = \Delta \text{turn} = 0$.

Variable	Description
Flaps	Degree of extension of the flaps in the segment.
TAS	True airspeed during the segment.
Altitude	Altitude at which the segment takes place.
Time	Time spent in the segment.
Distance	Distance covered in the segment.
Thrust	Engine thrust during the segment.
Pressure	Pressure difference at the segment altitude.
Mass	Aircraft mass during the segment.
%CMA	Relative position of the aircraft center of gravity with respect to the mean aerodynamic chord.
ZFW	Zero fuel weight of the aircraft.
PL	Payload weight.
FW	Fuel weight.

Table A.10: Description of the 12 scalar flight parameters $\mathbf{P} \in \mathbb{R}^{12}$ for each segment

Appendix A.2. Split

As stated in subsection 2.3, for each PSE, five missions were selected for training, one for validation and one for testing. However, in this phase, each {segment, PSE} constitutes a sample. This implies that, for each PSE, all the segments belonging to the five training missions are samples in the training set, and all the segments belonging to the validation

Stress Component	Description
$1g$	Equilibrium stress at the studied PSE corresponding to steady flight.
$\Delta_{V\text{man}}$	Incremental stress caused by a $1.5g$ vertical maneuver at the studied PSE.
$\Delta_{V\text{gust}}$	Incremental stress caused by a $1.5g$ vertical gust at the studied PSE.
Δ_{Turn}	Incremental stress caused by a $1.5g$ turn at the studied PSE.

Table A.11: Description of the four stress components $\mathbf{S} \in \mathbb{R}^4$ for each segment

and test missions belong to the validation and test sets respectively. This yields the split presented in Table A.12

	Train size	Validation size	Test size
Flight segments	1644	310	344
Ground segments	380	76	76

Table A.12: Set sizes for Phase I.

Appendix A.3. Input, output variables and model architecture

We shall distinguish in a separate way the input variables of $f_1^{\text{ground|PSE}}$ and f_1^{flight} . During ground segments (i.e. `taxi`) the wing is mainly subjected to gravity loads (the weight of the wing itself, the engine and the weight of the fuel stored in the wings). Since the wing and engine are the same across all the missions, for each PSE only one feature is the input variable to the model $f_1^{\text{ground|PSE}}$: FW.

For flight segments (i.e. `climb`, `cruise`, `descent`, `approach`), wings are also subjected to aerodynamic loads, so more variables will impact on stresses (for instance, lift is proportional to TAS²). So the following set of features are used as input variables for f_1^{flight} : {PSE (binary encoded), Flaps, Altitude, TAS, Mass, FW, Thrust}. All of them were normalized with a regular MinMax Scaler.

Likewise, the sole output variable of each $f_1^{\text{ground|PSE}}$ is $1g$, whereas for flight segments, the model outputs the equilibrium stress and the incremental stresses ($1.5g's$) caused by vertical gusts, vertical maneuvers and turns at the PSE, i.e. a four-dimensional output vector ($1g, \Delta_{V\text{man}}, \Delta_{V\text{gust}}, \Delta_{\text{Turn}}$).

Finally, the hyperparameters of the deep neural network used to approximate f_1^{flight} and other optimization parameters are depicted in Table A.13. Hyperparameter tuning was performed manually on the validation set to ensure generalization.

Train/Val/Test size	1664/310/344
Hidden layer sizes	50/50
Activation Function	ReLU
Loss Function	MAE
Optimizer	Adam
Weights initialization	Xavier
Learning rate α	$8 \cdot 10^{-3}$
Epochs	1000
Regularization	None
Mini batch Size	256
Scheduler: γ , Step	0.975, 30

Table A.13: Hyperparameters and optimization choices for the deep MLP used to approximate the stress properties for any given PSE for flight segments (f_1^{flight}).

Appendix B. Phase II: Additional details for Phase II

Appendix B.1. Data preprocessing

Predicted stresses from all the mission segments are averaged to form

$$\bar{\mathbf{S}}_{\text{ground}} = \langle 1g \rangle \in \mathbb{R}$$

for ground segments and

$$\bar{\mathbf{S}}_{\text{flight}} = (\langle 1g \rangle_{\text{flight}}, \langle \Delta v_{\text{man}} \rangle_{\text{flight}}, \langle \Delta v_{\text{gust}} \rangle_{\text{flight}}, \langle \Delta \text{turn} \rangle_{\text{flight}}) \in \mathbb{R}^4$$

for flight segments. In addition, the durations associated with each mission segment are used to compute t_{flight} and t_{ground} . All the averages $\langle \cdot \rangle$ above are computed in a similar way: as an example, the averaged equilibrium stress during flight segments

$$\langle 1g \rangle_{\text{flight}} = \frac{1}{t_{\text{flight}}} \sum 1g_i \cdot t_i,$$

where $1g_i$ and t_i are the predicted equilibrium stress of flight segment i and its duration, respectively.

Appendix B.2. Database

Load cycles: For each segment, load cycles caused by vertical maneuvers, gusts, and turns are included. In addition, the n GAG cycles corresponding to the n flights are also included. As detailed in subsection 2.1, these are stored as a vector with three components: Maximum stress, Minimum stress and Number of occurrences (after n flights). The associated damage for each of these cycles is also available (for the four k_t values).

Appendix B.3. Split

As stated in subsection 2.3, for each PSE, five missions were selected for training, one for validation and one for testing (with their respective four k_t values). In this phase, every $\{\text{mission, PSE, } k_t\}$ represents a sample. After filtering extreme values and unrealistic data, the set sizes for the GAG model and the gusts and maneuvers model are presented in Table B.14.

Table B.14: Set sizes

	Train size	Validation size	Test size
GAG	621	125	123
Gusts and maneuvers	533	104	107

Appendix B.4. f_2^{GAG} : input, output variables and model specs

f_2^{GAG} takes 9 numerical input variables: $k_t, \bar{\mathbf{S}}_{\text{flight}} \in \mathbb{R}^4, \bar{\mathbf{S}}_{\text{ground}}, n, t_{\text{flight}}, t_{\text{ground}}$. Note that as only wing PSEs are studied and all the wing PSEs have the same material, the material is not an input variable. The physical rationale behind each one of these input variables is as follows:

- k_t : The stress concentration factor, k_t , has a strong detrimental effect on fatigue life. This variable quantifies the amplification of local stress caused by defects or geometric characteristics, such as holes or joints. High k_t values promote crack nucleation. It is defined as:

$$k_t = \frac{\text{Local maximum stress}}{\text{Nominal stress}} \quad (\text{B.1})$$

and it is a key variable in this problem.

- $\langle 1g \rangle_{\text{ground}}$ and $\langle 1g \rangle_{\text{flight}}$: about the form and amplitude of the GAG cycle.
- $\langle \Delta v_{\text{gust}} \rangle, \langle \Delta v_{\text{man}} \rangle, \langle \Delta \text{turn} \rangle$: these averaged incremental stresses provide information about the magnitude of the stress oscillations caused by gusts and maneuvers. In the GAG cycle, the maximum stress will always be greater than $\langle 1g \rangle_{\text{flight}}$. The same happens with the minimum stress.
- $n, t_{\text{flight}}, t_{\text{ground}}$: These variables have a statistical impact. Longer flights increase the likelihood of encountering greater gusts or executing more demanding maneuvers, which augments the amplitude of the GAG cycle and, consequently the average GAG damage, \mathcal{D}_{GAG} , which is the output of the model. Besides, since the number of samples is finite, n is included to account for potential deviations from the true mean damage.

Input and output variables were normalized with MinMax Scaler and a logarithm was applied to the damage due to the scale difference between samples.

Finally, the specs of the MLP model and its hyperparameters are shown in Table B.15. Hyperparameter tuning was performed manually with the validation set to ensure generalization.

Train/Validation/Test sizes	621/125/123
Hidden layer sizes	64/64
Activation Function	tanh
Loss Function	MAE
Optimizer	Adam
Weights initialization	Xavier
Learning rate α	$8 \cdot 10^{-3}$
Epochs	5000
Regularization	Dropout, 0
Mini batch Size	128
Scheduler: γ , Step	0.975, 30

Table B.15: Specifications and hyperparameters of the MLP of f_2^{GAG} .

Appendix B.5. $f_2^{\text{G&M}}$: input, output variables and model specs

In this case we only have 7 input variables: $k_t, \bar{\mathbf{S}}_{\text{flight}} \in \mathbb{R}^4, n, t_{\text{flight}}$. The rationale of each variable is similar to that for f_2^{GAG} ; $\langle 1g \rangle_{\text{flight}}$ shows the stress level around which the oscillations that cause this damage take place. The magnitude of these oscillations is captured by $\langle \Delta \text{gust} \rangle, \langle \Delta \text{vman} \rangle, \langle \Delta \text{turn} \rangle$ and n, t_{flight} have the same statistical impact. Besides, longer flights typically imply more gusts encountered and maneuvers executed (not necessarily larger) and consequently greater damage. The output variable is the per-flight damage $\bar{\mathcal{D}}_{\text{G&M}}$, such that the cumulated damage is simply $\mathcal{D}_{\text{G&M}} = n \cdot \bar{\mathcal{D}}_{\text{G&M}}$. Once again, variables were normalized with MinMax Scaler and logarithm was applied to the damage. The MLP specs and hyperparameters are specified in Table B.16. Hyperparameter tuning was performed manually with the validation set to ensure generalization.

Table B.16: MLP architecture

Train/Validation/Test size	533/104/107
Hidden layer sizes	64/64
Activation Function	ReLU
Loss Function	MAE
Optimizer	Adam
Weights initialization	Xavier
Learning rate α	$8 \cdot 10^{-3}$
Epochs	5000
Regularization	Dropout, 0.001
Mini batch Size	128
Scheduler: γ , Step	0.975, 30

References

- [1] H. J. Grover, Fatigue of Aircraft Structures, Battelle Memorial Institute; Naval Air Systems Command, Department of the Navy, Washington, D.C., 1966.
- [2] European Union Aviation Safety Agency (EASA), Easy Access Rules for Large Aeroplanes (CS-25) (2023).
URL <https://www.easa.europa.eu/en/document-library/easy-access-rules/online-publications/easy-access-rules-large-aeroplanes-cs-25>
- [3] D. J. Linse, R. F. Stengel, Identification of aerodynamic coefficients using computational neural networks, *Journal of Guidance, Control, and Dynamics* 16 (6) (1993) 1018–1025. doi:10.2514/3.21122.
- [4] S. Suresh, S. N. Omkar, V. Mani, T. N. Guru Prakash, Lift coefficient prediction at high angle of attack using recurrent neural network, *Aerospace Science and Technology* 7 (8) (2003) 595–602. doi:10.1016/S1270-9638(03)00053-1.
- [5] N. R. Secco, B. S. d. Mattos, Artificial neural networks to predict aerodynamic coefficients of transport airplanes, *Aircraft Engineering and Aerospace Technology* 89 (2) (2017) 211–230. doi:10.1108/AEAT-05-2014-0069.
- [6] L. Lacasa, A. Pardo, P. Arbelo, M. Sánchez-Domínguez, N. Bascones, P. Yeste, A. Martínez-Cava, G. Rubio, I. Gómez, E. Valero, J. de Vicente, Towards certification: A complete statistical validation pipeline for supervised learning in industry, *Expert Systems with Applications* 277 (2025) 127169. doi:10.1016/j.eswa.2025.127169.
- [7] A. Alguacil, M. Bauerheim, M. C. Jacob, S. Moreau, Predicting the propagation of acoustic waves using deep convolutional neural networks, *Journal of Sound and Vibration* 512 (2021) 116285. doi:<https://doi.org/10.1016/j.jsv.2021.116285>.
- [8] M. Rüttgers, S.-R. Koh, J. Jitsev, W. Schröder, A. Lintermann, Prediction of acoustic fields using a lattice-boltzmann method and deep learning, in: H. Jagode, H. Anzt, G. Juckeland, H. Ltaief (Eds.), *High Performance Computing*, Springer International Publishing, Cham, 2020, pp. 81–101. doi:10.1007/978-3-030-59851-8_6.
- [9] D. Ramos, L. Lacasa, E. Valero, G. Rubio, Aerodynamic and structural airfoil shape optimisation via transfer learning-enhanced deep reinforcement learning, *arXiv preprint arXiv:2505.02634* (2025).
- [10] S. Le Clainche, E. Ferrer, S. Gibson, E. J. Cross, A. Parente, R. Vinuesa, Improving aircraft performance using machine learning: A review, *Aerospace Science and Technology* 138 (2023) 108354. doi:10.1016/j.ast.2023.108354.
- [11] A. Graziani, D. Prederi, A. A. Trezzini, M. Favale, P. Masarati, Prediction of helicopter rotor loads and fatigue damage evaluation with neural networks, *Aerotecnica Missili & Spazio* (2024). doi:10.1007/s42496-024-00226-4.

[12] J. J. Valdés, C. Cheung, A. L. Rubio, Extreme learning machines to approximate low dimensional spaces for helicopter load signal and fatigue life estimation, in: 2017 International Joint Conference on Neural Networks (IJCNN), 2017, pp. 1991–1998. doi:10.1109/IJCNN.2017.7966095.

[13] K. Palczynski, D. Skibicki, L. Pejkowski, T. Andrysiak, Application of machine learning methods in multiaxial fatigue life prediction, *Fatigue & Fracture of Engineering Materials & Structures* 46 (2) (2022) 416–432. doi:10.1111/ffe.13874.

[14] D. Chen, Y. Li, K. Liu, Y. Li, A physics-informed neural network approach to fatigue life prediction using small quantity of samples, *International Journal of Fatigue* 166 (2023) 107270. doi:10.1016/j.ijfatigue.2022.107270.

[15] J. Zhang, J. Zhu, W. Guo, W. Guo, A machine learning-based approach to predict the fatigue life of three-dimensional cracked specimens, *International Journal of Fatigue* 159 (2022) 106808. doi:10.1016/j.ijfatigue.2022.106808.

[16] H. B. Younis, K. Kamal, M. F. Sheikh, A. Hamza, Prediction of fatigue crack growth rate in aircraft aluminum alloys using optimized neural networks, *Theoretical and Applied Fracture Mechanics* 117 (2022) 103196. doi:10.1016/j.tafmec.2021.103196.

[17] EASA, Daedalean, Concepts of design assurance for neural networks (codann), Tech. rep., technical report (3 2020).
 URL <https://www.easa.europa.eu/sites/default/files/dfu/EASA-DDLN-Concepts-of-Design-Assurance-for-Neural-Networks-CoDANN.pdf>

[18] EASA, Daedalean, Concepts of design assurance for neural networks (codann) ii with appendix b, Tech. rep. (1 2024).
 URL <https://www.easa.europa.eu/en/document-library/general-publications/concepts-design-assurance-neural-networks-codann-ii>

[19] I. Goodfellow, Y. Bengio, A. Courville, Y. Bengio, Deep learning, Vol. 1, MIT press Cambridge, 2016.

[20] Department of Defense, USA, MIL-A-8861B – Military Specification: Airplane Strength and Rigidity – Flight Loads (February 1986).

[21] R. B. Bland, A. A. Putnam, Discussion: “Cumulative Damage In Fatigue” (Miner, M. A., 1945, ASME J. Appl. Mech., 12, pp. A159–A164), *Journal of Applied Mechanics* 13 (2) (1946) A169–A170. doi:10.1115/1.4009555.

[22] B. Eiximeno, B. Begiashvili, A. Miro, E. Valero, O. Lehmkuhl, pylom: Low order modelling in python (2022).
 URL https://github.com/ArnauMiro/UPM_BSC_LowOrder

- [23] A. Paszke, S. Gross, F. Massa, A. Lerer, J. Bradbury, G. Chanan, T. Killeen, Z. Lin, N. Gimelshein, L. Antiga, et al., Pytorch: An imperative style, high-performance deep learning library, in: Advances in Neural Information Processing Systems (NeurIPS), 2019, pp. 8024–8035.
- [24] F. Pedregosa, G. Varoquaux, A. Gramfort, V. Michel, B. Thirion, O. Grisel, M. Blondel, P. Prettenhofer, R. Weiss, V. Dubourg, J. Vanderplas, A. Passos, D. Cournapeau, M. Brucher, M. Perrot, E. Duchesnay, Scikit-learn: Machine learning in Python, *Journal of Machine Learning Research* 12 (2011) 2825–2830.
- [25] W. McKinney, Data structures for statistical computing in python, in: S. van der Walt, J. Millman (Eds.), *Proceedings of the 9th Python in Science Conference*, 2010, pp. 51–56.
- [26] C. R. Harris, K. J. Millman, S. J. van der Walt, R. Gommers, P. Virtanen, D. Cournapeau, E. Wieser, J. Taylor, S. Berg, N. J. Smith, R. Kern, M. Picus, S. Hoyer, M. H. van Kerkwijk, M. Brett, A. Haldane, J. F. del Río, M. Wiebe, P. Peterson, P. Gérard-Marchant, K. Sheppard, T. Reddy, W. Weckesser, H. Abbasi, C. Gohlke, T. E. Oliphant, Array programming with NumPy, *Nature* 585 (7825) (2020) 357–362. [doi:10.1038/s41586-020-2649-2](https://doi.org/10.1038/s41586-020-2649-2)
URL <https://doi.org/10.1038/s41586-020-2649-2>
- [27] J. D. Hunter, Matplotlib: A 2d graphics environment, *Computing in Science & Engineering* 9 (3) (2007) 90–95. [doi:10.1109/MCSE.2007.55](https://doi.org/10.1109/MCSE.2007.55).
- [28] F. W. Scholz, M. A. Stephens, K-sample anderson–darling tests, *Journal of the American Statistical Association* 82 (399) (1987) 918–924.
- [29] J. Hodges Jr, The significance probability of the smirnov two-sample test, *Arkiv för matematik* 3 (5) (1958) 469–486.